

Special Section:

Exploring planetary caves as windows into subsurface geology, habitability, and astrobiology

Key Points:

- We reconstructed the morphology of five lunar pits, and derived a degradation sequence for pits
- Mare pits formed significantly after emplacement of their host mare
- Pit morphology presents significant exploration challenges; a low-cost precursor mission would benefit future pit exploration

Correspondence to:

R. V. Wagner,
rvwagner@asu.edu

Citation:

Wagner, R. V., & Robinson, M. S. (2022). Lunar pit morphology: Implications for exploration. *Journal of Geophysical Research: Planets*, 127, e2022JE007328. <https://doi.org/10.1029/2022JE007328>

Received 6 APR 2022

Accepted 28 JUL 2022

Author Contributions:

Conceptualization: R. V. Wagner, M. S. Robinson

Data curation: R. V. Wagner

Formal analysis: R. V. Wagner

Funding acquisition: M. S. Robinson

Investigation: R. V. Wagner

Methodology: R. V. Wagner, M. S. Robinson

Project Administration: M. S. Robinson

Resources: M. S. Robinson

Software: R. V. Wagner

Supervision: M. S. Robinson

Validation: R. V. Wagner

Visualization: R. V. Wagner

Writing – original draft: R. V. Wagner

Writing – review & editing: R. V. Wagner, M. S. Robinson

Lunar Pit Morphology: Implications for Exploration

R. V. Wagner¹  and M. S. Robinson¹

¹School of Earth and Space Exploration, Arizona State University, Tempe, AZ, USA

Abstract Lunar pits are small (~10–300 m wide) collapse features with vertical walls and sometimes overhangs. We have identified almost 300 pits, mostly in ponds of cooled impact melt inside large craters younger than ~1 billion years. Several of these pits may provide access to lava tubes or other caves, and those in the maria expose the layering record of the top 20–100 m of basaltic lava flows. We investigated the 21 known pits outside of impact melt ponds to determine possible origins, ages, and present-day access to the lunar subsurface. We used Lunar Reconnaissance Orbiter Narrow Angle Camera images (<2 m per pixel) to produce detailed 3D reconstructions of six pit interiors. We evaluated the general morphology and geologic context of all twenty-one. While four pits have contexts suggestive of lava tubes, the majority are ambiguous, although all occur in or near the maria. We also propose that pit formation is an ongoing process, as the degree of degradation of a pit is unrelated to the age of the host terrain. Much of the original volume of most pits is now filled with debris, but some exhibit significant overhangs and may have present-day cave access. Viewing pit walls and floors, even from the rims, requires navigating steep slopes of loose material. Since the floors are also covered with rough debris piles, we recommend simple flying vehicles for initial reconnaissance.

Plain Language Summary Lunar pits are small (~10–300 m wide) collapse features with cliff-like vertical walls, and sometimes overhangs, and may provide access to lava tubes or other caves. Most of the almost three hundred known pits are in impact melt ponds of craters, but those outside craters may connect to larger cave systems and, in the maria, expose the layering record of a significant period of lunar volcanic activity. We investigated the origins and accessibility of pits in the lunar maria and highlands and used Lunar Reconnaissance Orbiter Narrow Angle Camera images to reconstruct the interiors of six pits. While 4 of the 21 studied pits suggest lava tubes, the majority have no compelling evidence for any specific type of underlying cave. We also propose that pits open up over time, exposing ancient void spaces, and erode over hundreds of millions of years. Most pits are unlikely to have present-day cave access due to infilling by debris, but some have large confirmed overhangs and may open into caves. Viewing pit interiors from the surface and traversing the interiors require navigating steep slopes, loose material, and large boulders, so we recommend flying vehicles for initial pit exploration.

1. Introduction

Lunar pits are an unusual negative relief landform characterized by near-vertical walls and inward-sloping rims, hypothesized to be formed by collapse into a pre-existing tectonically- or volcanically-derived subsurface void (Haruyama et al., 2009; Wagner & Robinson, 2014). Similar features occur on Mars (Cushing, 2012, 2015; Cushing et al., 2007, 2015). On Earth, features that appear similar in aerial imagery include pit craters and lava tube skylights (Okubo & Martel, 1998; Sauro et al., 2020).

We have run a campaign to identify lunar pits using images from the lunar reconnaissance orbiter camera (LROC) narrow angle camera (NAC), which collects nadir images of the lunar surface with typical pixel scales of 0.5–2 m (Robinson et al., 2010; Wagner & Robinson, 2014). There are currently 16 known pits in the lunar maria, along with almost 300 pits in impact melt ponds, and five pits in the lunar highlands unassociated with any impact craters (Haruyama et al., 2009; Wagner & Robinson, 2014, 2019, 2021; Wagner et al., 2017; Yokota et al., 2018).

Most of the mare and highland pits and approximately half of the impact melt pits were identified using *PitScan*, a semi-automated search tool that detects shadows that may be associated with pits (Wagner & Robinson, 2014, 2018). The remaining impact melt pits were either found incidentally during other research or identified through manual inspection of melt ponds in which *PitScan* found pits. Most new pit discoveries since Wagner and Robinson (2014) are mare pits, suggesting that most remaining unknown impact melt pits are smaller than the detection threshold for *PitScan* in recent NAC images (~25 m pit diameter).

In this work, we investigate the geologic context of lunar mare and highland pits to constrain their possible formation mechanisms, which will constrain the shape and scope of any currently unobservable subsurface voids. Additionally, we use off-nadir NAC images with pixel scales ranging from 0.26 to 2.2 m to investigate pit interiors. Where multiple viewing angles are available with similar lighting, we use stereo models to characterize the morphology of the pit walls and floors. Finally, we discuss the implications of these morphologies for potential landed exploration.

2. Background

Caves on the Moon have been theorized since at least the mid-twentieth century, with lava tubes in particular theorized as potentially being common in the lunar maria (Greeley, 1971; Halliday, 1966; Heacock et al., 1966; Hörz, 1985). The first known lunar pit, hypothesized to be an opening into a lava tube, was discovered in the Marius Hills region from Kaguya images (6–12 m pixel scale), with two more pits identified the next year (Haruyama et al., 2009, 2010). LROC NAC observations followed up those first discoveries with higher-resolution (down to ~0.5 m pixel scale) showing details of pit morphologies and revealing hundreds of additional pits (Robinson et al., 2012; Wagner & Robinson, 2014).

We now know that most pits on the Moon occur in impact crater melt ponds, with almost 300 impact melt pits found to date (Wagner & Robinson, 2021). Pits in the maria are much rarer, with only 16 identified, although they also tend to be much larger. Additionally, five pits were identified in non-impact-melt terrain outside of, although usually close to, the bounds of lunar maria. Note that we have reclassified two previously described pits from mare to highland, Schlüter and Southwest Fecunditatis, after reevaluating their locations relative to mare boundaries. The current list of known mare and highland pits, including abbreviated names used in this work, is summarized in Table 1. Full details of all known pits, including impact melt pits, are published in the LROC Planetary Data System (PDS) archive as the product SHAPEFILE_LUNAR_PIT_LOCATIONS, also available in an interactive catalog at <http://lroc.sese.asu.edu/pits> (Wagner & Robinson, 2021).

Previous work has described the general morphology of pits. Wagner and Robinson (2014) broke down lunar pits into a steep-walled inner pit surrounded by a sloping funnel, while Cushing et al. (2015) proposed a pit classification based on floor shape and overhang morphology for Martian Atypical Pit Craters (APCs). Figure 1 shows our current schematic cross-section of a generalized lunar pit, informed by these prior works and the observations in this work (see Section 6). We retain the general division of a funnel surrounding a vertical-walled depression from Wagner and Robinson (2014), but now explicitly include the funnel in the pit depth, and have adopted a floor and overhang morphology similar to the Type II APCs of Cushing et al. (2015) as our baseline for lunar mare and highland pits.

There are two compelling scientific and exploration rationales for investigating pit formation mechanisms. First, pits provide access to a cross-section of the underlying bedrock exposed in pit walls. In mare pits in particular, this exposure enables direct access to layers of mare flow units, allowing investigation of the history of lunar volcanism without extensive drilling operations (Nesnas et al., 2019; Robinson et al., 2012). Additionally, intercalated regolith layers may contain records of solar-wind-implanted species across a broad range of solar history (Fagents et al., 2010).

Second, and the focus of this study, is the potential for accessing lunar caves (in this work, we use “cave” to refer to any sublunarean void space that is physically connected to a pit, regardless of scale or origin; see Mylroie (2019)). Lunar caves could preserve delicate structures for billions of years, and pits or caves could provide shelter for modern-day explorers, making them attractive destinations from both scientific and engineering perspectives. In a hypothetical lunar cave, the environment is benign, with no danger from micro- (or even most macro-) meteorites, little if any radiation exposure (De Angelis et al., 2002; Turner & Kunkel, 2017), and a constant temperature near 15°C (Horvath et al., 2022). Even without a cave, the exposure to micrometeorites and radiation can be significantly reduced at the bottom of a pit (Wagner et al., 2017), although the thermal environment on a pit floor may be harsher than the surrounding surface (Horvath et al., 2022).

To determine what types of caves may be accessible from lunar pits, we look to theories about what form those underlying void spaces might take. Several hypotheses for the formation of mare and highland pits exist: (a) skylights into active lava tubes; (b) recent roof collapse into an ancient lava tube; (c) stoping of the ceiling of

Table 1
Mare and Highland Pits on the Moon

Location/Name	Latitude (°N)	Longitude (°E)	Diameter (m)	Depth (m)	Terrain	Terrain age (Ga)	Degradation state
Central Mare Fecunditatis	−0.917	48.660	122 × 100	>45	Mare	3.5	3–4
Compton	56.224	106.195	110 × 92	>57	Mare	3.6	3
Lacus Mortis (LMP)	44.962	25.610	>165 × 110	115	Mare	—	3
Lacus Mortis 2	44.815	25.201	~290 × 270 ^a	~115	Mare	—	5+
Mare Ingenii (MIP)	−35.948	166.053	104 × 71	100	Mare	—	2–3
Mare Insularum	8.687	330.965	>165 × 159	>50	Mare	3.0	5
Mare Moscoviense	29.503	150.465	180 × 170 ^a	~35 ^b	Mare	2.6	4
Mare Tranquillitatis (MTP)	8.336	33.222	100 × 88	133	Mare	3.6	2
Marius Hills (MHP)	14.091	303.230	55 × 49	60	Mare	—	2
North Procellarum 1	35.408	314.360	157 × 108	~65	Mare	—	3–4
North Procellarum 2	35.343	314.345	160 × 135 ^a	~45	Mare	—	4
Runge Crater	−2.702	86.780	14 × 12	5 ^b	Mare	3.1 ^c	2
Serenitatis	35.104	17.402	21 × 17	>22 ^b	Mare	3.4	2
Sinus Iridum	45.623	331.189	66 × 32	~35	Mare	3.4	3
Southwest Tranquillitatis	4.145	24.686	32 × 26	~55	Mare	3.6	1–2
West Marius Hills	13.551	301.827	>50 × 47	~12 ^b	Mare	—	4
Highland 1	43.966	23.083	41 × 37	~25	Highland	—	3
Highland 2	41.156	18.819	34 × 27	~25	Highland	—	3–4
Highland 3	42.394	320.307	45 × 41	28	Highland	—	4
Schlüter Crater (SCP)	−5.839	276.950	37 × 23	~80	Highland	—	1
Southwest Mare Fecunditatis (SWFP)	−6.752	42.759	19 × 15	~80	Highland	—	1

Note. Diameters are measured parallel and perpendicular to the longest axis of the pit, from inner rim to inner rim where both rims exist. Depth is measured from surrounding horizontal surface to lowest measured point, potentially under an overhang, and includes the funnel where possible. Ages are for the mare unit in which the pit is formed (Hiesinger et al., 2011), not the age of pit formation. Degradation states are defined in Section 7; larger numbers are more degraded.

^aPit is close to circular; diameters found by fitting an ellipse to points on the inner rim, and measuring between inner rims along the resulting major and minor axes. ^bDepth does not include funnel. ^cPit lies just outside of Hiesinger et al. age unit, but in similar terrain.

a near-surface intrusive magmatic structure; and (d) collapse into tectonic voids (Haruyama et al., 2009, 2010; Robinson et al., 2012; Wagner & Robinson, 2014).

The lunar maria have long been theorized to contain extensive lava tubes (Coombs & Hawke, 1992; Greeley, 1971; Halliday, 1966; Hörz, 1985), perhaps much longer and with greater diameters than those found on Earth due to

both the high discharge rate of lava and the low lunar gravity. Recent modeling has suggested that lava tubes up to 3.5 km wide could be mechanically stable on the Moon (modeled with a 3:1 width: height ratio), although it should be noted that the same analysis allows for terrestrial lava tubes up to 800 m wide, while the largest known terrestrial lava tube is ~30 m wide (Blair et al., 2017). Simple gravitational scaling (Blair et al., 2017) of that largest terrestrial tube would still suggest lunar lava tubes with ~200 m wide, however, and prior mapping has shown probable collapsed lunar lava tube segments on the scale of 200–400 m wide (Coombs & Hawke, 1992; Hörz, 1985). There have been suggestions of an intact lava tube between the two Marius Hills pits from gravity (Chappaz et al., 2017) and radar (Kaku et al., 2017) observations, but these identifications are tentative. In active terrestrial lava tubes, small collapses of lava tube roofs result in openings known as skylights; partial roof collapses that post-date the eruptive phase may also be referred to as skylights. Skylights provide ready access

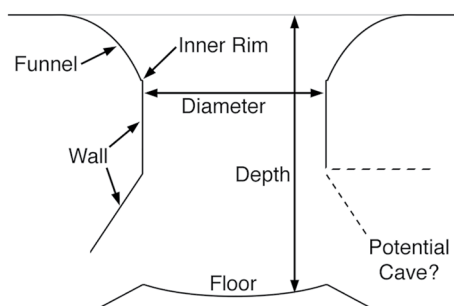


Figure 1. Schematic cross-section of a generic pit. Not all pits exhibit all of these features, or show these shapes. See Section 6 for a detailed description of pit features.

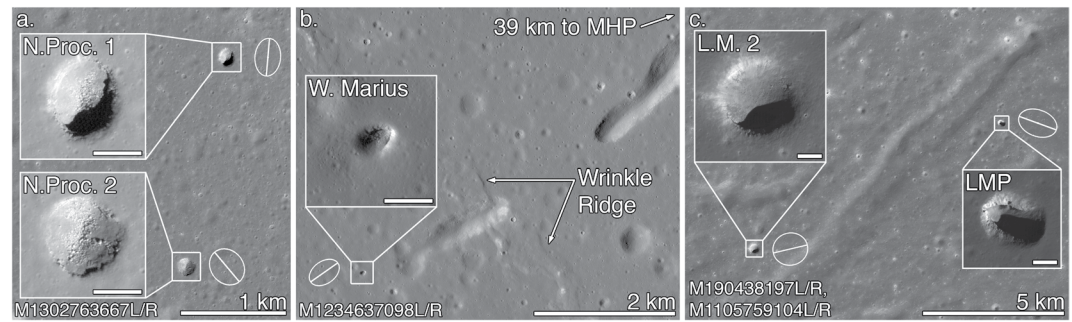


Figure 2. (a) The North Procellarum pit pair. (b) The West Marius Hills pit and nearby collapse features suggestive of a lava tube. (c) The Lacus Mortis pit pair and Rimae Bürg. Ellipses show pit orientation and ellipticity, line marks long axis. Scale bars in all inset enlargements are 100 m.

to portions of the remaining tube, no matter their formation time. Since lava tubes and skylights are common in terrestrial basaltic flood basalts, and there is circumstantial evidence for lava tubes on the Moon, it is natural to hypothesize that the mare pits are openings to such voids, and thus the lunar examples have been referred to as skylights (e.g., Haruyama et al., 2009).

Intrusive magmatism (magma chambers, dikes, etc.) can create subsurface volcano-tectonic voids as magma intrudes along fault planes dilating the host rock (Wilson et al., 2011). A terrestrial example of this is the cave connected to the Wood Valley Pit Crater in Hawai'i, which extends over 200 m, and is accessible through a collapse pit similar in appearance to many lunar pits (Favre, 1993; Okubo et al., 2013). Alternate mechanisms, such as ceiling collapse into purely tectonically formed voids (Okubo & Martel, 1998; Wyrick, 2004), could produce pits without requiring a large or accessible cave system (a terrestrial example of this may be the Devil's Throat pit crater in Hawai'i).

3. Geologic Context and Formation of Lunar Pits

Understanding the nature of lunar pits is hampered by the inability of current orbital assets to definitively probe the subsurface at relevant scales. The best we can do is compare these orbital observations with terrestrial analogs, make inferences about formation mechanisms, and use these inferences to determine the optimal strategy to design future missions to obtain relevant measurements from within pits.

A standard method of identifying likely lava tubes from aerial observations on Earth and Mars is the presence of linearly- or sinuously-aligned pits, usually elliptical with long axes following the path of the inferred (or mapped, on Earth) underlying cave (Sauro et al., 2020). However, only two pairs of mare pits are close enough together to use this method. The North Procellarum 1 and 2 pits occur two km apart near the Mairan volcanic complex. These could reasonably be collapse pits into a single lava tube or other linear void space, as the more elliptical of the two (North Procellarum 1) has a long axis oriented roughly parallel to the line between them, although the other does not (Figure 2a).

The two mare pits in the Marius Hills volcanic complex could also be connected to lava tubes: The Marius Hills pit (MHP) is in the floor of a sinuous rille, and thus is known to be in a location where lava was channelized. The West Marius Hills pit, ~45 km west-southwest, is aligned with a linear collapse feature (~1.8 km long, ~0.4 km wide, and 50 m deep) ~1 km away that crosses a wrinkle ridge—potentially a lava tube segment collapsed by tectonic activity (Figure 2b). These two pits are unlikely to have collapsed into the same lava tube, however, due to the presence of an apparent vent structure between them.

One more pair of pits is potentially close enough to be connected to the same void space: the Lacus Mortis pits, ~10 km apart. These are unlikely to be connected to a single lava tube, however, as the long axis of the non-circular one is mostly perpendicular to the line between them, and they are separated by a graben, Rimae Bürg, with no sign of a collapsed tube (Figure 2c). Some relation to the local extensional tectonism is plausible, however.

With four pits showing evidence of association with lava tubes, we are left with the remaining 16 mare and highland pits. Of those, the only one with a strong indication of nearby volcanic activity (beyond the maria themselves) is the Serenitatis pit, which lies 700 m southwest of an apparent volcanic vent.

Several pits occur close to tectonic landforms. The Lacus Mortis pits are both located within a kilometer of a large graben, Rimae Bürg; the Southwest Tranquillitatis pit is ~ 2 km from the edge of a wrinkle ridge; the Runge pit is ~ 100 m from a lobate scarp, and two impact melt pits in Sharonov crater occur on the peak of a wrinkle ridge. Additionally, the Southwest Mare Fecunditatis pit (SWFP) lies in a region of extensional tectonism, ~ 8 km from a circumferential graben of Mare Fecunditatis. These cases could indicate that the underlying void space may be tectonic in origin, or that a pre-existing magmatic void was disrupted by tectonic activity. A point against the idea of tectonic activity triggering the formation of these pits is that we see a much larger disruption at the West Marius Hills pit where a tectonic structure crosses a presumed former void space (Figure 2b), suggesting that at other sites, whatever pre-existing void the pit opened into was small, deep, or did not cross the tectonic feature.

Three of the five highland pits lie within 10 km of an edge of a mare, and the remaining two are in a patch of highlands surrounded by the maria Serenitatis, Imbrium, Frigoris, and Lacus Mortis. All five highland pits were found via an automated search of images randomly distributed over the entire lunar surface (*PitScan*; Wagner & Robinson, 2014, 2018), so this proximity to maria is unlikely to be coincidental. This proximity suggests a possible origin through volcanic processes, perhaps dike formation from magmas that did not reach the surface during mare formation. The two pits furthest from a mare edge, Highland 1 and 2, are roughly aligned with the trend of the Rimae Bürg graben, although it is not visible near the pits, suggesting a possible tectonic component to their formation (Wagner & Robinson, 2014).

As all of the mare and highland pits are near maria, volcanically associated voids may be involved in their formation. However, the majority of these pits have no surface evidence of the void they formed into or how extensive it might be. To further constrain the nature of the underlying voids, it may be necessary to investigate the interiors of lunar pits. In the following sections, we will evaluate how much can be determined about pit interiors from current orbital observations.

4. Pit 3D Reconstruction

A complete morphometric understanding of the visible portion of pits provides the most reliable information for testing formation hypotheses. Key parameters include layering, planform shape, wall slopes, overhang extent, floor slope, roof thickness, and volume of collapsed materials. Here we examine all relevant NAC observations to create accurate three-dimensional models of six pits.

The Lunar Reconnaissance Orbiter (LRO) NAC consists of two line-scan cameras aimed side-by-side with a combined 5.7° FOV and a nominal pixel scale of 0.5 m from an altitude of 50 km above the mean lunar surface (Robinson et al., 2010). Since 2012, the spacecraft has been in an elliptical orbit where the apoapse altitude can be as high as 200 km in the northern hemisphere (pixel scale 2 m). LRO is in a polar orbit, so the direction of travel is generally within a few degrees of north-to-south, with orbit obliquity at $\sim 88^\circ$ as of 2022. As LRO is not in a Sun-synchronous orbit, the lighting varies from month to month, enabling imaging of various parts of a pit interior over time. The vast majority of NAC observations are nadir pointed; off-nadir observations are obtained by slewing the spacecraft. Roll slews are most common (east or west, with the sensor aligned to the plane of the rotation), but pitch slews (north or south direction) can be commanded if the target is directly under an orbital track. We have used only roll slews for quantitative measurements in this analysis, although pitch slew images of the Mare Tranquillitatis (MTP), Mare Ingenii (MIP), and Lacus Mortis (LMP) pits provide supporting context.

4.1. Monoscopic Analysis

From a single off-nadir image of a pit, it is possible to make inferences about the geometry of the walls based on what is and is not illuminated or occluded, and with basic trigonometric analyses derive a simple set of morphometric parameters. For example, the east wall of MTP below 60 m depth has not been imaged in stereo, but we constrained its overhang angle to $20\text{--}40^\circ$ using lighting geometry in two images (Figures 3a–3c). As a more complex example, the Schlüter highland pit (SCP) is texturally bland below the funnel, with no distinctive features (required for stereo analysis). However, we can still use off-nadir images to show that there is a point

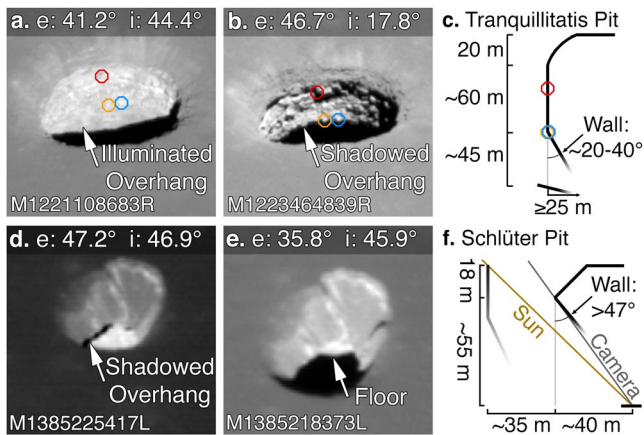


Figure 3. Monoscopic wall angle analyses. (a, b) Slew images of the east wall of Mare Tranquillitatis pit (MTP), with lower wall lit or shadowed depending on Sun angle. “*e*” is emission angle (between camera boresight and zenith), “*i*” is solar incidence angle in the same plane as the camera angle. Pit spans ~ 100 m left-to-right. (c) Cross-section of MTP, showing the angle constraint on the lower wall. (d) Slew image of the east side of Schlüter Crater pit (SCP), with shadowed overhang indicating a wall closer to horizontal than vertical. Funnel spans ~ 50 m left-to-right and ~ 55 m near-to-far. (e) Slew image of SCP, where coincidental alignment of the near edge of the illuminated floor and the far inner rim allows for a single-image measurement of that point on the floor, in conjunction with 3D modeling of the funnel. (f) Diagram of the scene in panel (e). North is to the left in all images; images are aspect-corrected to mimic a framing camera, see Section 4.2.2.

on the floor of the pit at approximately 59 ± 17 m below the funnel, and 43 ± 12 m laterally below the east rim, and that the pit has a ceiling immediately below the bottom of the eastern funnel that is at least 47° off-vertical (Figures 3d–3f). Error bars are based on ± 3 m uncertainty in distance from the near rim to point on the inner rim where the edge of the floor is visible, and ± 2 m uncertainty in the funnel depth.

4.2. Stereo Analysis

For several mare pits, LROC acquired multiple oblique views at different slew angles, often with similar lighting, providing off-nadir stereo pairs that allow the construction of a depth map of one or both walls. We modeled the walls of four mare pits and one highland pit using tools in the USGS *Integrated Systems for Imagers and Spectrometers* (ISIS) (Anderson et al., 2004; Laura et al., 2022) to manually create networks of matching points. We derived the 3D positions of those points using two methods: by trigonometrically solving for point position using a simplified geometry model, and by running the network through the ISIS *jigsaw* tool; a bundle-adjustment software that reports match point positions in 3D (Edmundson et al., 2012; Sides et al., 2017).

4.2.1. Reference DTMs

SOCET SET (commercial software from BAE Systems) is used by the LROC team to produce high-resolution DTMs (Henriksen et al., 2017). While we have not used *SOCET SET* to produce models of pit walls, we used updated *SOCET SET*-derived DTMs to align our wall point clouds. Most of these DTMs were carefully edited during processing to minimize erroneous points around the pit rims, and both the MIP and MTP DTMs include small sections of floor. We used these DTMs as “truth” surfaces for testing our models.

4.2.2. Preprocessing Steps

There are three major complications with locating stereo matches by direct comparison of two NAC oblique images:

1. As the NAC is a line-scan camera, image pixels are often not square; their down-track size varies with exposure time, while the cross-track size is a function of distance-to-target.
2. Due to the orbital configuration of LRO, a given NAC image may be flipped vertically, horizontally, or both relative to a map view.
3. Most potential oblique stereo observations of pit walls were not intentionally acquired as stereo and have varying lighting and resolution.

Additionally, as the obliquity of the orbit has changed over the mission, the angle between the y-axis of the raw image and north has changed, and so two images not taken on the same day may be rotated several degrees relative to each other.

We corrected the first two issues through image-space adjustments to the data to produce “pseudo-framing-camera” images of a $\sim 500 \times 500$ pixel window around the pit. Non-square pixel aspect ratio was corrected by scaling each image in the down-track direction to match the cross-track pixel scale when projected on a plane perpendicular to the boresight, and all images were flipped to an approximate north-up, east-right orientation. These corrections made manual selection of match points faster and more accurate, as the images could thus be directly viewed in stereo.

Lighting and resolution differences, along with the orbit obliquity, could not be corrected via pre-processing, and they prevented automatic feature matching in most cases. Manual point matching was usually still possible, especially when the only significant difference was resolution; lighting and obliquity changes made manual matching more difficult, and increased eyestrain (Figures 4d–4f).

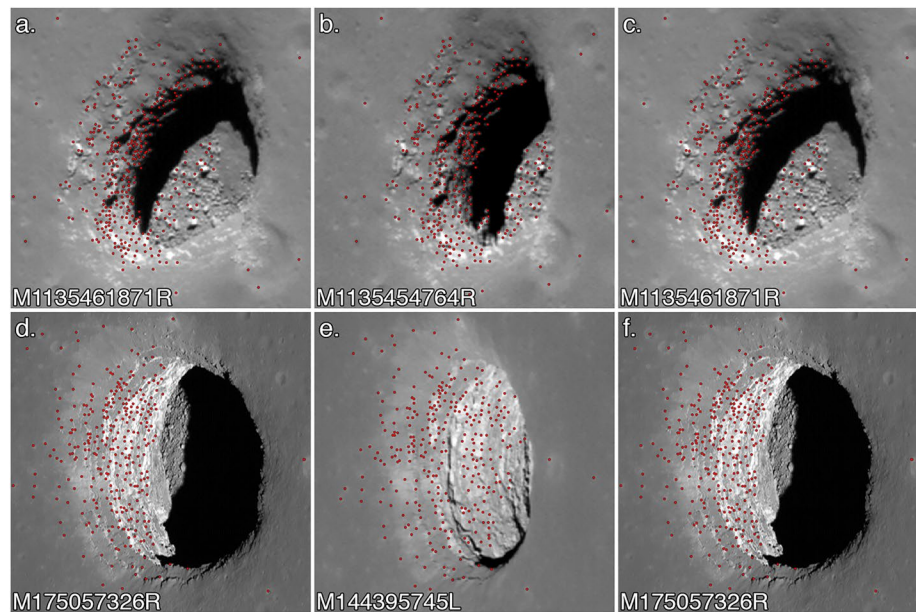


Figure 4. (a–c) Match points for the west wall of Mare Ingenii pit. These images were intentionally acquired as stereo, and are similar enough that automated point matching succeeded on the surrounding mare. The resulting model is presented in Figure 6d. (d–f) Match points for the west wall of Mare Tranquillitatis pit, a pair with large differences in resolution and viewing angle, preventing automated point matching and making manual viewing difficult. Panels a and c are identical, as are d and f, to allow for multiple stereo viewing modes: left pair for parallel viewing, right pair for convergent (“cross-eyed”) viewing.

4.2.3. Manual Control Network Creation

Our primary method of creating control networks was to load both images into the ISIS control network editing tool *qnet*, zoom them to the same scale, and place them in a side-by-side arrangement suitable for cross-eyed free-viewing of the images (Figure 4). We then placed each match point on an identifiable feature in one image and tweaked the position in the other image by 0.125–0.5 pixel increments until the displayed marker appeared flush against the lunar surface in 3D. We estimate the accuracy of point placement at ~ 0.5 pixels in the lower-resolution image. Point spacing averaged ~ 4 pixels (4–10 m), depending on density of high-contrast features. Each network also contains at least three alignment control points where we have also measured the selected features' positions on a NAC DTM of the site (where available), to allow tying multiple models together.

In two cases (SCP and SWFP), we did not have NAC DTMs. We used a single alignment control point at each of these sites to tie the models together. As jigsaw returns point positions in body-fixed lunar $x/y/z$ coordinates, we automatically rotated each model to match our Y -north, Z -up local coordinate system using the vector from the center of the Moon to the alignment control point before translating the models to match each other. Comparing this alignment method to the fully controlled point clouds for the pits with DTMs (LMP, MHP, MIP, MTP), individual stereo models are rotated by up to 1° relative to their fully controlled counterparts and are usually translated by several meters. Overall, the SCP and SWFP models are well enough controlled to evaluate their morphology, and the main loss from not having a DTM is the lack of dense surface points surrounding the pits.

4.2.4. Automated Control Networks

For stereo pairs with similar lighting and pixel scale, we attempted to reduce the manual effort required with an initial control network using the ISIS tool *findfeatures* (Sides et al., 2017). All resulting automatic match points were manually verified. In general, automatic point matches worked well on smooth horizontal surfaces, but required significant manual adjustment on vertical pit walls. Automated matching also required much closer lighting, pixel scale, and slew angle similarity than successful manual match point selection (Figure 4).

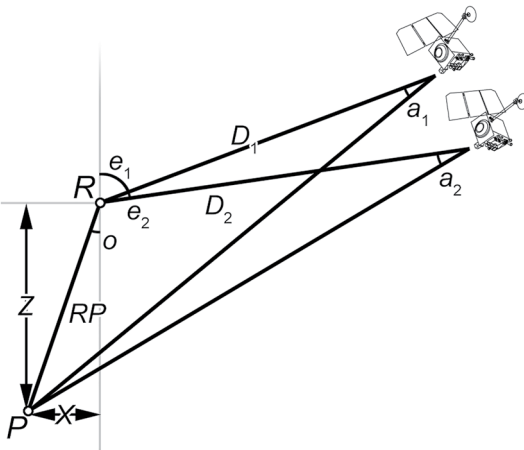


Figure 5. Illustration of the trigonometric problem for the location of point P relative to point R using an oblique stereo pair. e_1 and e_2 are emission angles from a zenith-pointing vector to the camera, and D_1 and D_2 are the distance between the surface and the camera. These values are known from spacecraft ephemeris. a_1 and a_2 are measured from the image data (distance in pixels from the match point to the image column that contains the reference point), using known camera parameters to convert cross-track pixel distances to angles. Overhang angle o and positions X and Z are the unknowns to be found; distance RP is a useful intermediate value. Diagram is not to scale.

4.2.5. Jigsaw Solution

To convert the control networks of X/Y positions of point in image space into $X/Y/Z$ positions in a lunar reference frame, we used ISIS *jigsaw* bundle-adjustment software. We set *jigsaw* to only correct the camera pointing, not the position, as the impact of the expected $\sim 10\text{--}20$ m spacecraft uncertainty was negligible.

As ISIS automatically compensates for scaling transformations when calculating spacecraft position and pointing information, the aspect-correction scaling does not affect the output from *jigsaw*. Flipping is not automatically handled, so we tracked that operation and edited our control network files as needed to invert the control point pixel coordinates before passing them to *jigsaw*.

Jigsaw's output includes the $X/Y/Z$ position of each match point in the lunar reference frame. We converted this to local coordinates by shifting the point cloud to minimize offsets between the alignment control points in *jigsaw*'s output and their measured locations from the reference DTM.

4.2.6. Trigonometric Solution

Jigsaw was not specifically intended for this usage, so we developed a simplified trigonometric method of producing 3D models of pits as a sanity check. Using the assumptions that the orbit tracks of any two images are parallel and that the recorded spacecraft positions are exactly correct (close to true, given LRO's polar orbit with $>88^\circ$ inclination and <25 m positional uncertainty (Mazarico et al., 2018), but these assumptions are expected to introduce small errors, discussed below), we construct a 2D trigonometric problem in the plane observed by a single line of an image to derive the relative positions in local $X/Y/Z$ coordinates of each match point and an arbitrary point on the rim (Figure 5). The reference point may or may not appear in the same line of the image as any match points, but the assumption of parallel orbit tracks, and small distances involved, allows us to treat the reference point as if it is in every line of the image at the same cross-track position, for the purposes of calculating cross-track and vertical offsets (effectively, we consider it a reference line running down-track at a fixed cross-track and vertical position).

We start with a Law of Sines equality based on the shared side of the two triangles, the overhang line RP between the reference point R and the point P being measured (Figure 5):

$$RP = D_1 \times \frac{\sin(a_1)}{\sin(e_1 - a_1 - o)} = D_2 \times \frac{\sin(a_2)}{\sin(e_2 - a_2 - o)} \quad (1)$$

This can be solved for o via some manual manipulation and the WolframAlpha solver (Wolfram Alpha LLC, 2017) to become:

$$o = \text{atan} \left(-\frac{D_1 * \sin(a_1) * \sin(e_2 - a_2) - D_2 * \sin(a_2) * \sin(e_1 - a_1)}{D_2 * \sin(a_2) * \cos(e_1 - a_1) - D_1 * \sin(a_1) * \cos(e_2 - a_2)} \right) \quad (2)$$

Once the overhang angle o has been found, the X position (cross-track direction, perpendicular to gravity) and Z position (parallel to gravity) can be trivially found relative to the reference point R . To calculate the down-track position of a match point, we multiplied the down-track pixel scale by the number of lines separating the match point from the reference point. This method produces slightly distorted results due to the not-fully accurate assumption of parallel orbit tracks, but provides a simple, verifiable model to test other methods against.

4.2.7. Error Estimation

We estimate that point placement accuracy is $\pm \sim 0.5$ native-scale pixels in the higher resolution image (the point coregistration was done on images enlarged to $\sim 2\times$ native pixel scale to take maximum advantage of cases where the down-track pixel scale was better than the cross-track).

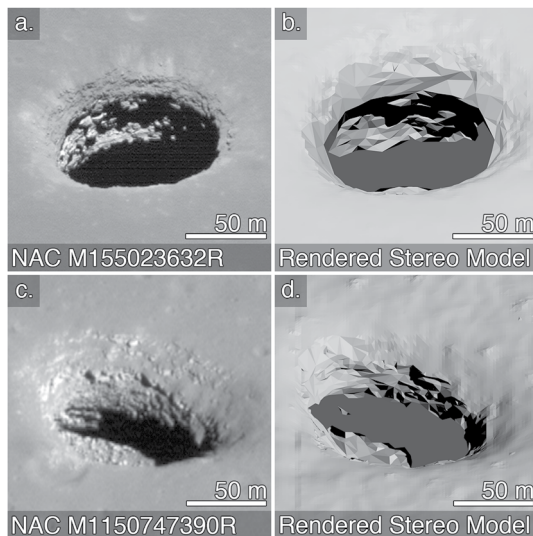


Figure 6. (a) Mare Tranquillitatis pit (MTP) east wall imaged with grazing sunlight. (b) Our model of MTP, merged with a narrow angle camera DTM of the surrounding surface, rendered with very similar lighting and viewing angles. Note the missing rocks on the left-hand side of the wall in the render, due to insufficient modeled points. (c) Mare Ingenii pit (MIP) west wall image. (d) Our model of MIP, with similar viewing parameters.

To evaluate the impact of point placement uncertainty on the final model, we varied the pixel coordinate inputs into the trigonometric code by the estimated accuracy. Higher convergence angles reduced the uncertainty in the vertical direction, while lower emission angles reduced cross-track uncertainty. Vertical uncertainty due to point-matching error was 1–10 m for models of walls (median 6 m), and 5–18 m for models of floors (median 6 m), due to the lower available convergence angles with good floor coverage. Cross-track uncertainty was 0–10 m for all models (median 2 m). We found that a convergence angle of 20° and average emission angle of ~40° struck the best balance between low uncertainty and ease of identifying features on vertical surfaces in both images.

4.2.8. Verification

The *jigsaw* and trigonometric methods produce very similar wall geometries: when the *jigsaw* and trigonometric models from a given stereo pair are aligned via Iterative Closest Point matching (ICP; CloudCompare, 2019), the median point-to-point offset is <1.6 m at all sites, indicating that the internal geometry of both models is generally accurate over the ~100 m span of a pit wall. The *jigsaw* models, however, are better aligned to each other than are the trigonometric models, and also appear to align better to the reference DTMs. This is likely due to distortions in the trigonometric model (from oversimplifications such as assuming parallel orbit tracks) that have a larger effect over the few hundred meters separating the alignment control points than within the modeled surface, leading to higher absolute control uncertainty. This is particularly noticeable in the floor of MTP (125 m below the

surface), where two stereo reconstructions overlap the sliver of floor included in the reference DTM, including two locations where a match point in each model is placed on the same end of an identifiable block, and thus should match nearly perfectly. The trigonometric models do not overlap the reference DTM, and the two points that should match are separated from each other by ~40 m, while both *jigsaw* models overlap as expected, with offsets between those same matching points of ~1.2 m. This is likely a result of *jigsaw* more accurately handling differences in orbital inclination.

As an additional qualitative verification of the wall modeling, we produced triangle meshes from the wall point clouds from *jigsaw*, merged with NAC DTMs of the surrounding surface, and rendered “synthetic NAC images” using the 3D modeling software *Blender* (Blender Online Community, 2018) with matching lighting, viewing, and camera parameters to actual NAC pit images. *Blender* only supports framing camera models, but the visible difference between framing and line-scan cameras is minimal with this large focal length and tiny image area. Comparing the synthetic images to NAC images that were not involved in the creation of the models (where available) indicates that the overall geometry is correct. However, small features such as 5–10 m wide rocks are sometimes absent when not readily identifiable in the original stereo images (Figure 6).

As an additional quantitative test, we produced a model of a terrestrial pit crater using synthetic NACs of a high-resolution 3D model of that pit (Wagner & Robinson, 2019) with the same imaging parameters, including resolution, as the images we used to model MTP. We aligned the low-resolution point clouds from *jigsaw* for each wall to the original model via the ICP algorithm and measured the distance between the two point clouds using the software *CloudCompare* (CloudCompare, 2019). The overall RMS error was 65 cm (80 cm east wall, 40 cm west wall), with no correlation between *X/Y/Z* position and error, indicating that our 3D modeling method produces dimensionally accurate models, with errors on the order of the source image pixel scale.

5. Observed Pit Morphologies

Our point clouds of the interiors of the modeled pits are shown in Figure 7, and a summary of the models and observations is given in Table 2. In the descriptions below, all depths are measured from the mean level of the surface surrounding the pit, outside the funnel. All overhang angles are given as degrees from vertical. Point

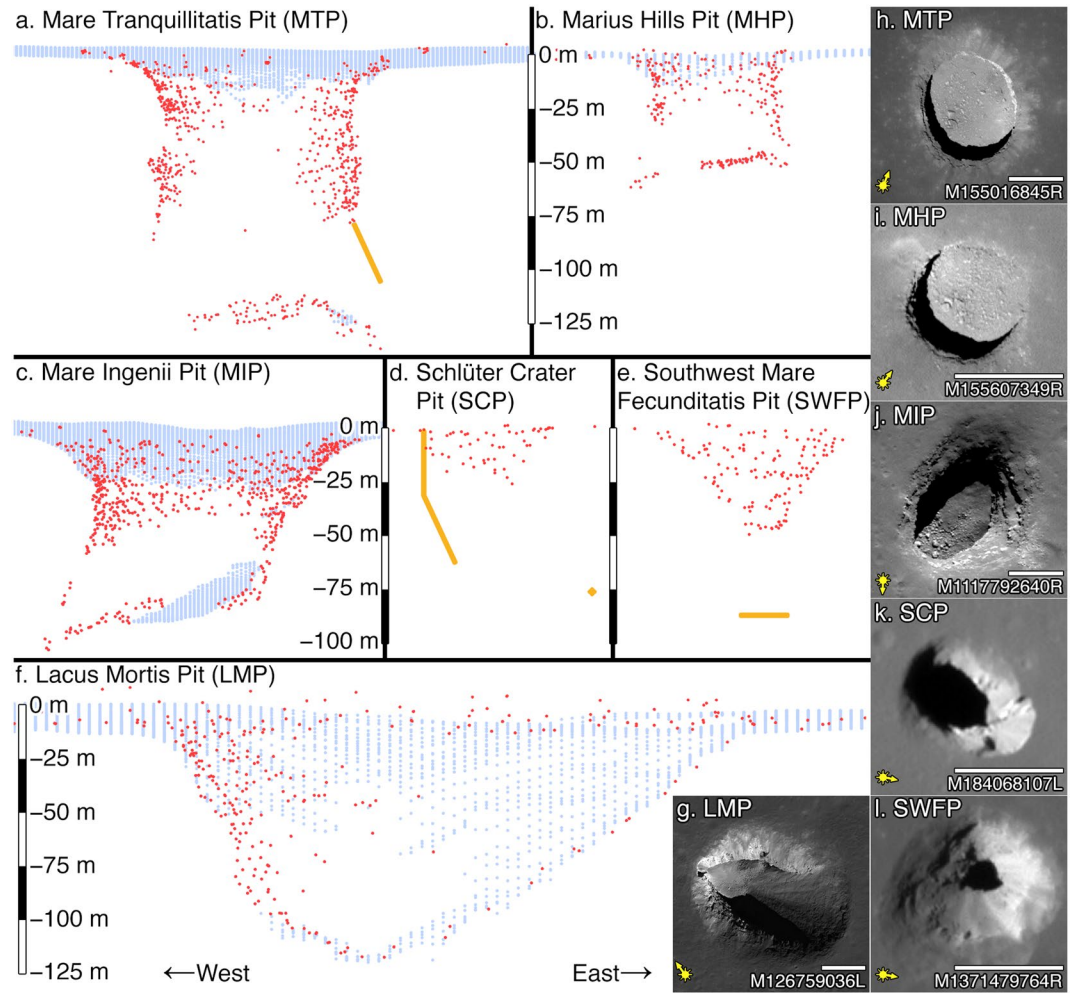


Figure 7. (a–f) Side views of the full 3D point clouds, from the south. All point cloud panels are in the same scale; vertical and horizontal scales match. Light blue dots (often appear as vertical lines due to density) are from Narrow Angle Camera DTMs, red are from this work. Orange lines are approximate locations of wall and floor surfaces from monoscopic analysis; these features are not included in the archived point clouds. (g–l) Nadir views of each pit. Illumination direction is marked with Sun symbol; scale bar in each panel is 50 m.

cloud files suitable for viewing in 3D display software (.OBJ files) are available in the Zenodo data archive associated with this paper (Wagner & Robinson, 2022).

5.1. Mare Tranquillitatis Pit (MTP)

On the west side, the funnel slope increases smoothly, transitioning to vertical wall between ~ 15 and ~ 30 m depth. The wall has a large alcove (~ 23 m high, inset > 6 m from the rim) starting at 33 m depth, which is also visible to a lesser extent on north and east walls, and is overhung $\sim 10^\circ$ below that. Wall morphology is poorly constrained below ~ 80 – 90 m depth. On the east side, the funnel is ~ 30 m deep, with average slope increasing from $\sim 35^\circ$ to $\sim 65^\circ$ at the first coherent layer at ~ 15 m depth. There is an abrupt increase in albedo at the transition to vertical at 30 m depth. The wall is vertical ($\pm \sim 15^\circ$) to ~ 80 m depth, then overhung 20 – 40° below 80 m. There is a high point on the floor at 115 m depth under the northeastern rim, with downward slopes toward the center of the pit and under the eastern overhang. The floor is covered with unsorted blocks, with larger blocks (up to ~ 10 m) partially embedded in finer-grained material, although pixel-scale (30–100 cm) texturing suggests that the finer-grained material may consist largely of blocks tens of centimeters in size. To the north, there is a protruding layer on the wall at 80 m depth, visible in nadir-looking images, and the floor extends at least 8 m under the north rim.

Table 2
Summary of Reconstructed Pits

Pit	General shape	Stereo model details	Uncertainty
MTP	Nearly cylindrical, vertical to overhung walls. Overhangs to north, east, and west.	7 pairs, 732 points	± 3 m X, ± 1 m Y, ± 4 m Z, except west-central floor is ± 9 m Z
MHP	Nearly cylindrical, vertical to overhung walls. Overhang to west.	4 pairs, 240 points	± 4 m X, ± 1 m Y, ± 4 m Z
MIP	Elliptical. East wall sloped, others vertical to overhung. Floor slopes down from northeast to southwest, possibly meeting back wall under overhang.	2 pairs, 681 points	± 3 m X, ± 1 m Y, ± 3 m Z
SCP	Elliptical. Funnel is large on east, almost absent on west. Pit has large void space to east, and near-vertical wall on west.	2 pairs, 89 points, funnel only, no DTM	± 1 m X, ± 1 m Y, ± 3 m Z
SWFP	Nearly triangular pit, very large circular funnel. Overhangs on east and west.	2 pairs, 139 points, funnel only, no DTM	± 2 m X, ± 1 m Y, ± 4 m Z (± 12 m Z on west side)
LMP	Elliptical. West wall is vertical, east wall is gradual slope from rim to bowl-shaped floor, north wall has overhang.	2 pairs, 395 points, mostly covers west wall	± 2 m X, ± 2 m Y, ± 7 m Z

Note. Uncertainty is for worst stereo pair except where noted. X direction is east-west, Y direction is north-south.

5.2. Marius Hills Pit (MHP)

The western funnel ranges from almost absent to the northwest (where the pit cuts through the floor of a ~ 15 m diameter crater) to ~ 10 m deep to the southwest. The crater on the rim appears to have ordinary, fairly crisp morphology, apart from being truncated by the rim of MHP ~ 4 m from its center, and there is a sharp protrusion on the wall of MHP just below the crater. The west wall of MHP is roughly vertical to 30 m depth, then turns inward with an overhang of 20° – 50° . The western floor is at ~ 60 m depth. The eastern funnel is ~ 5 m deep. The eastern wall is overhung $\sim 5^\circ$, starting immediately below the funnel, and meets the floor at 50 m depth in a ~ 5 m recessed alcove. The high point of the floor is under the eastern rim, and the floor slopes downward to both east and west, with indications of a bowl shape toward the center of the pit, and a uniform appearance of meters-scale blocks embedded in material with sub-pixel (< 50 cm) grain size.

5.3. Mare Ingenii Pit (MIP)

The western funnel extends down, with some outcrops, to a coherent rim layer at ~ 23 m depth. Below that point, the wall starts out vertical, then curves to become overhung by a depth of ~ 55 m. Most points below that are hidden in shadow in existing images, but there is a visible outcrop at 80 m depth to the southwest, and the lowest visible portion of the floor is at 100 m, with a possible wall-floor contact visible behind it. A slewed image looking south shows an overhang under the southern rim. The eastern funnel has a shallow slope, reaching a first coherent layer at ~ 13 m depth. The wall below that layer exhibits a series of stairsteps, each with ~ 5 – 10 m of vertical wall and up to ~ 5 m of regolith-covered slope. From the base of the northeast wall, at ~ 60 m depth, the floor slopes down at $\sim 25^\circ$ to a level region that starts ~ 30 m from the southwest rim; this slope is covered in fine-grained material. The floor below the fine-grained slope is mostly covered in 1–5 m blocks, and resumes its $\sim 25^\circ$ slope in the overhung areas, still covered in blocks.

5.4. Schlüter Crater Pit (SCP)

The west wall shows only a small expression of a funnel above a near-vertical to slightly overhung wall to ~ 20 – 30 m depth. That wall transitions to a nearly featureless sloped surface ($\sim 60^\circ$ – 75° off-horizontal) that continues to at least 60 m depth. The funnel is more developed on the east side, and is ~ 18 m deep, with an average $\sim 45^\circ$ slope (there is a break in slope at ~ 8 m depth, with shallower slopes above, ~ 30 – 45° , and steeper below, ~ 45 – 60°). At the southeast end of the pit is an unbroken slope from inner rim up to a ~ 3 m tall wall at the surface of the regolith. The bottom of the funnel is a sharp transition to an extreme overhang ($> 45^\circ$ from vertical). A single point on the floor has been measured, at ~ 80 m (± 20 m) depth under the overhang.

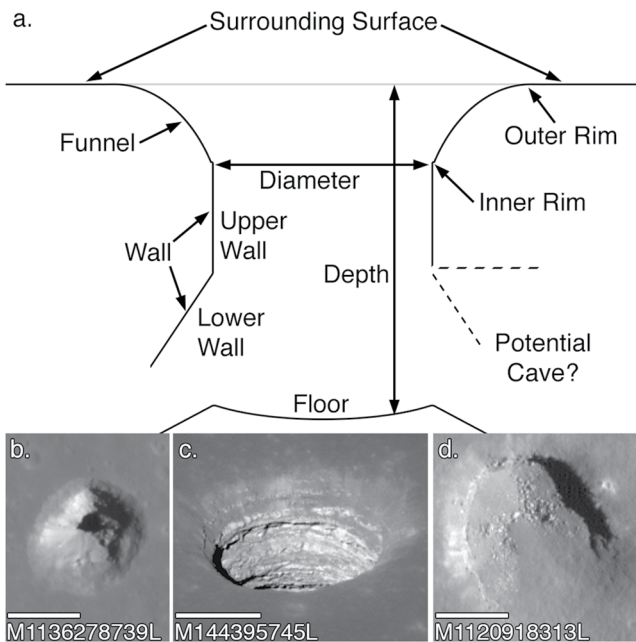


Figure 8. (a) Schematic cross-section of a generic pit. Not all pits exhibit all of these features, or show these shapes. Note that inner rim is exaggerated for visibility. (b) Southwest Mare Fecunditatis pit, illustrating a large funnel. (c) Mare Tranquillitatis pit west wall, illustrating wall and funnel, viewed from 51° off-nadir. (d) Central Mare Fecunditatis pit, illustrating a bowl-shaped floor. Scale bar in each panel is 50 m.

5.5. Southwest Mare Fecunditatis Pit (SWFP)

This highland pit lies on a $\sim 7^\circ$ slope trending downward from southwest to northeast. The funnel is 35–45 m deep. The average slope on the north and east sides is $\sim 55^\circ$, while on the south and west the slope is $\sim 45^\circ$. There is a bright layer exposed ~ 30 m above the bottom of the funnel, which may also be a few-meter-high vertical face at many points. Numerous other protrusions and ledges occur in the funnel below this layer, although they have no visible albedo signature and can only be detected from shadowing. The inner opening of the pit is about 15×15 m. The floor is ~ 40 m below the inner rim and appears to extend under overhangs on both the east and west sides; there are no identifiable blocks in the parts of the floor we have been able to observe, nor have any walls been imaged.

5.6. Lacus Mortis Pit (LMP)

The eastern side of the pit is relatively featureless and slopes from the surrounding mare surface to the floor, $\sim 21^\circ$ off horizontal. The western end of the pit consists of a 35 m wide, ~ 75 m high notch, with a debris pile against the wall underneath extending the rest of the way to the lowest point of the bowl-shaped floor at ~ 115 m depth. Along the northern rim, the funnel increases from nearly absent at the west end to ~ 50 m deep where it meets the eastern slope, although the transition from funnel to wall is poorly defined along the entire length. The only visible overhang is under the northern rim, with the wall transitioning from upward-facing to overhung at ~ 60 m depth. There is a mound on the northern floor, extending into the overhung region, under a ~ 30 m wide divot in the northern wall/funnel. Blocks on the floor are sorted, with very few on the eastern slope, and none > 1 m on the western slope. The northern mound has blocks up to ~ 2 m, mostly partially buried, and the floor between these sloped regions is filled with free-standing 1–3 m blocks.

6. Pit Anatomy

From these detailed analyses, and observations of other mare and highland pits, we can create a general model of the interior morphology (Figure 8a). We will discuss these from outside to inside: funnel, walls, floor, overhangs, and potential for there being a significant roofed void or cave.

6.1. Funnel

Lunar pits exhibit a sloping funnel for all or nearly all their circumference that extends inward from the surrounding surface down to a near vertical wall. Typically the funnel exhibits a gradually increasing slope approaching the pit, from nearly horizontal at some distance from the pit, to a maximum slope just above the vertical walls. The beginning of this slope (“outer rim” in Figure 8a) is rarely easy to identify. We do not have a strict definition for the bottom of the funnel (transition to vertical walls), but there is often a mostly continuous coherent layer at the top of the vertical wall that casts shadows suitable for taking depth measurements, sometimes with a sharp transition (Figure 8b). Where this “inner rim” exists, we use it to define the bottom of the funnel. Otherwise, we generally use the first extensive vertical surface that is more than a couple of meters high. This means that the funnel can encompass small non-continuous or non-vertical outcrops of coherent material, which may contribute to the frequent presence of average funnel slopes significantly above the angle of repose (slopes $> \sim 36^\circ$; Wagner et al., 2013). For example, the bottommost portion of the eastern funnel of MTP exceeds 60° . In some cases, however, there are no visible layers, indicating that the funnel consists of material stable at slopes above 36° .

We have measured slopes up to 60° in the funnel of SCP (as well as the near-vertical wall at surface level on the southeast end), with the average slope being 45° , well above the $\sim 36^\circ$ angle of repose of unconsolidated regolith

(Wagner et al., 2013). Similarly, SWFP has funnel slopes significantly over 36° , even along lines without visible ledges. The subsurface of the highland terrain at these locations is expected to be regolith, or similarly broken-up material (Cintala & McBride, 1995). Our results indicate that this material is cohesive enough to be stable at slopes $>45^\circ$ over long periods. This cohesiveness may be similar to that seen when the Apollo astronauts dug trenches with nearly vertical walls in the upper ~ 10 cm of regolith, but on a larger scale and stable over a timescale of at least the 10 years over which we have LROC NAC images of SCP and SWFP. It is unclear what would create an inner rim of a pit in this terrain, but an alignment of multiple blocks within the regolith might produce a solid rim; this hypothesis is consistent with the disparity in inner rim depths between the two sides of SCP.

Blocky outcrops occur within the funnels of the MIP and MTP mare pits starting at 6 and 12 m depth, respectively, with the uppermost continuous layer around 20 m depth at both pits. This depth is largely consistent with the expected mare regolith depths of deeper than 8–32 m (cf. Wilcox et al., 2005). However, overall funnel depths can vary widely, even around the rim of a single pit (e.g., MHP, LMP), which may indicate influence from deeper local fracturing from impacts that may pre-date the pit formation, independent of the average regolith depth.

6.2. Walls

The walls of mare pits often exhibit a break in slope; the upper wall is usually roughly vertical, and the lower wall overhung. The upper walls have significant meter-scale roughness, and numerous near-horizontal partings (interpreted as flow boundaries). Due to the limited range of lighting and viewing angles and occurrences of overhangs, it is rarely possible to characterize the morphology of the lower walls.

We note that the five highland pits may not generally share the same characteristics as the mare pits. The Highland 1–3 pits all have very little exposed wall, with almost all of their depth coming from their funnels and bowl-shaped floors. SCP has one vertical wall and one steeply overhung ceiling with no visible wall, and the inner rim of SWFP, on both east and west, appears similar to the overhung ceiling of SCP. These may indicate two distinct classes of pit, with Highland 1–3 being more similar to drainage pit craters (e.g., Rima Hyginus; Wilson et al., 2011), and SCP and SWFP perhaps being young examples of the same morphology as most mare pits.

The partings in mare pit walls are identifiable by both morphology and reflectance. Near 0° phase (Sun and camera in line), alternating relatively high and low reflectance bands are seen (although these are rarely circumferentially continuous), while with more grazing light, the partings are highlighted by shadows (compare left and right sides of Figure 8c). We interpret the reflectance banding as due to fine grained regolith particles that collected on upward-facing surfaces (fallen from above or flung by nearby impacts), while surfaces that are vertical or downward-facing are generally cleaner and brighter.

6.3. Floors

Pit floors generally appear to consist of a mix of sizes of blocks, ranging from >10 m to below the detection limit of NAC images (~ 0.5 – 1.0 m). Most visible blocks are <2 m in diameter. There are frequently sloped sections of pit floors, with a high point against a wall or underneath a rim, and a downward slope going toward the middle of the floor. Where this occurs, the slope has very few discrete blocks visible on the slope in 0.5 – 1.0 m pixel scale images, and a region of densely packed blocks at the base (see east, west, and northeast sides of LMP, and northeast side of MIP; Figure 7). This distribution is consistent with a sorting regime for floor material where new material falls at the edge, larger blocks roll away, and finer-grained material largely stays put. Over time this sorting process results in a bowl-shaped floor with a field of blocks in the middle (e.g., Figure 8d).

Based on shading, MTP and MHP appear to exhibit flat floors, with most large blocks partially buried by finer-grained material in the floor. However, in our 3D reconstructions, both pits show a ridge under their eastern rims, sloping down at 10 – 15° toward the centers of the floors, and 20 – 30° under the eastern overhangs, for a total observed relief of 10 – 20 m (the western floors of these pits have not been imaged in stereo). The difference between shading and stereo results may be due to the floors only being illuminated near noon. This pattern of floor slopes with peaks directly beneath the rim has also been seen in Type II Atypical Pit Craters on Mars (Cushing et al., 2015) and in a terrestrial pit crater (Wagner et al., 2018). This morphology is not unexpected, as if most infill comes from erosion of the rim and vertical walls, it will pile up underneath them, not in the center of the pit or beneath any overhangs. It does mean that nadir images showing a bowl-shaped floor that appears to

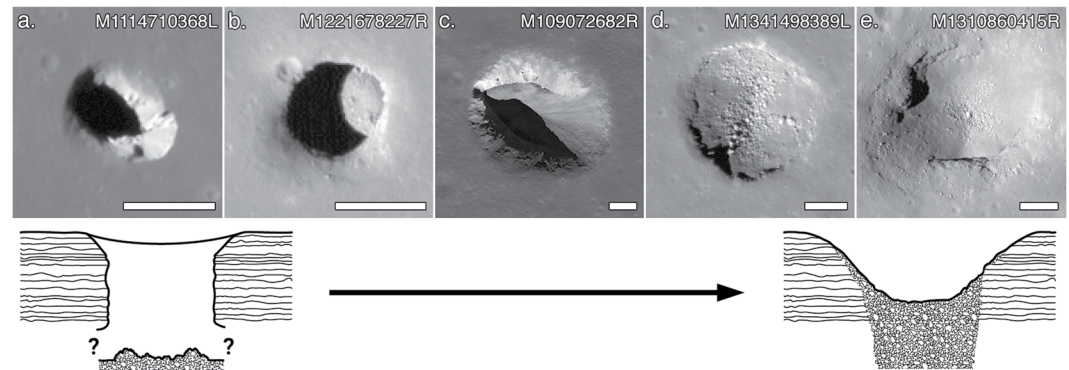


Figure 9. Examples of pits exhibiting a range of degradation states, from nearly pristine (degradation state 1; a) to highly degraded (state 5; e). (a) Schlüter Crater pit. (b) Marius Hills pit. (c) Lacus Mortis pit. (d) North Procellarum 2 pit. (e) Mare Insularum pit. Scale bars are 50 m, all panels have similar incidence angles. Bottom half shows notional cross-sectional view of the degradation end-members.

rest against the wall cannot be used to determine whether a pit has overhangs: there could be another downward slope underneath a hypothetical overhang, hidden by the rim. Off-nadir observations are necessary to confirm or rule out overhangs.

Regolith grains thrown into a pit will accumulate on the floor and infill around the large blocks. It is not known if this infill would be fast enough to smooth out the rough surface from falls of larger rocks, though the paucity of wholly unburied blocks in MTP and MHP suggests that infill by fines may be significant, at least in deeper pits.

Our current reconstruction of floor morphology is too uncertain to identify topographic details at scales smaller than ~20–30 m. Identifiable points are largely limited to sharp edges at the tops of blocks, so the floor between blocks is not well modeled, and there is added variance in the “floor” measurement from the varying heights of the blocks. Additionally, for deep, narrow pits such as MTP and MHP, a given spot on the floor can only be seen in stereo with narrow convergence angles, which increases reconstruction uncertainty (our central floor models have 7°–9° convergence, while ~25° is optimal (Henriksen et al., 2017)).

7. Formation Age and Mechanisms of Evolution Over Time

Definitively determining the formation mechanism for mare pits in general (or for each pit) is not possible with the existing observations. However, inferences can be made based on the morphometric analysis presented in this work combined with knowledge of the age of host mare unit, lunar degradation rates, and similar features found on Earth.

7.1. Degradation State

Lunar mare pits exhibit a range of morphologies, from large depth-to-diameter ($d:D$) ratios and floors that appear generally flat, with most of the depth coming from the funnel and vertical or overhung walls, to low $d:D$ ratios with bowl-shaped floors, and much of the depth coming from the bowl shape of the floor (Figure 9). There is likely a continuum between these two types, with pits becoming wider, shallower, and more bowl-shaped over time as their edges are worn away by small impacts and their interiors are infilled. A similar transition was documented in the Devil's Throat pit crater in Hawai'i (Okubo & Martel, 1998), albeit on a much shorter timescale and with terrestrial erosion mechanisms.

We propose a degradation scale based on observed pit morphologies:

1. Distinct upper boundary of funnel and/or sudden overhang under the funnel with no identifiable vertical wall.
2. All walls are vertical or overhung, floor appears relatively flat.
3. As category 2, but with one wall having collapsed, resulting in a floor-to-surface ramp, and/or bottom appears clearly bowl-shaped.
4. Bottom is bowl-shaped and contributes more to the depth than any remaining vertical wall.

5. As category 4, but with multiple ramps from surrounding surface to floor.

Beyond category 5, pits are largely indistinguishable from impact craters or other depressions. Pit degradation states are included in Table 1.

Only two pits are in degradation category 1 (SCP and SWFP, Figures 7k and 7l), both in highland terrain, so it is not clear if the “distinct funnel boundary” and “sudden overhang” features are truly part of a continuous degradation sequence and would also appear in very fresh mare pits. Additionally, the Highland 1, 2, and 3 pits may have similarly crisp funnels (the resolution of available images is too low for unambiguous identification) despite otherwise falling into categories 3–4. This pattern of crisp funnels in highland pits may indicate that the funnel and wall shapes of highland pits are due to terrain, not age, with the thick highland regolith being more prone to collapsing to a uniform slope than mare regolith that may have shallower bedrock remnants.

Even very degraded pits can exhibit remnants of what we interpret was once a more extensive overhang: At the Mare Insularum pit (Figure 9e), the southeast wall has a ~2 m deep overhang, and shading on the terrain under that overhang suggests that it is sloped downward to the wall, with a peak ~1 m forward from the present-day rim.

The pits with the best exposures of vertical walls, and thus layering, lie in the middle of the morphology range (states 2–3, e.g., Figures 9b and 9c). Crisper pits tend to have significantly overhung walls and smaller openings, making observation difficult (although they may be more likely to have extant access to deeper void spaces), and more-worn pits have less remaining vertical exposure.

7.2. Formation Age

There is no correlation between pit degradation states and the age of the host terrain (Table 1). For example, the relatively crisp MTP occurs in a mare unit (3.6 Ga) older than the host mare unit (3.0 Ga) of the significantly degraded Mare Insularum pit. This lack of correlation is consistent with the argument made by Wagner and Robinson (2014) that most mare pits cannot be skylights formed at the time of lava tube emplacement due to pit diameters being significantly smaller than the equilibrium crater diameter for their host surfaces. The 15 m diameter crater cut by the MHP (noted above) is consistent with a relatively young age for pit formation. Craters of diameter 20 m are in equilibrium at ~300 my (Trask, 1966), and the 15 m crater is only moderately degraded, indicating that the pit opening formed, or expanded by ~5–10 m, within the last ~100 my. A more extreme example is the tiny Runge Crater pit, which at <15 m wide should have been obliterated several times over in the 3.1 billion years since the formation of its host mare, but still falls into degradation category 2, with vertical walls on all sides. These observations suggest that new pits are formed significantly after the local host maria were formed and, once open, degrade until they are largely indistinguishable from impact craters, consistent with the relative paucity of mare pits.

On the other end of the timescale, pits do not change significantly over decadal time scales. The Apollo Panoramic Imager (Masursky et al., 1978; Robinson et al., 2008) photographed MTP and SWFP during the Apollo 15 and 16 missions in 1971 and 1972 (MTP: photographs AS15-P-9846, AS15-P-9851; SWFP: photographs AS16-P-4478, AS16-P-4483), although if they were noticed at the time, these pits were apparently never documented. The Apollo images allow identification of features ~5 m across, and a comparison with NAC images taken 40-plus years later does not show any changes in rim shape or albedo streaking from landslides.

Impact crater density measured on pit floors indicates that pit interiors are resurfaced over geologically short timescales, likely by falling wall and funnel material, and debris from nearby impacts. We only identified six impact craters within lunar pits: five on the landslide in LMP (all ~2 m in diameter), and one 23 m diameter crater, nearly obscured by debris, in the Moscoviense pit (one of the shallowest mare pits).

We interpret that impact melt pits have a lifespan of <1 by, due to their almost exclusive occurrence in Copernican craters (Wagner & Robinson, 2014). However, that is an upper bound on the age of impact melt pits. There are pits in Copernicus and King crater impact melt deposits, ~800 ma and ~1 by old, respectively (Ashley et al., 2012; Heisinger et al., 2012), that do not appear significantly more degraded than pits in Tycho crater (~100 my old; Heisinger et al., 2012). Given these observations, we interpret that typical impact melt pits have a lifespan on the order of 100 my.

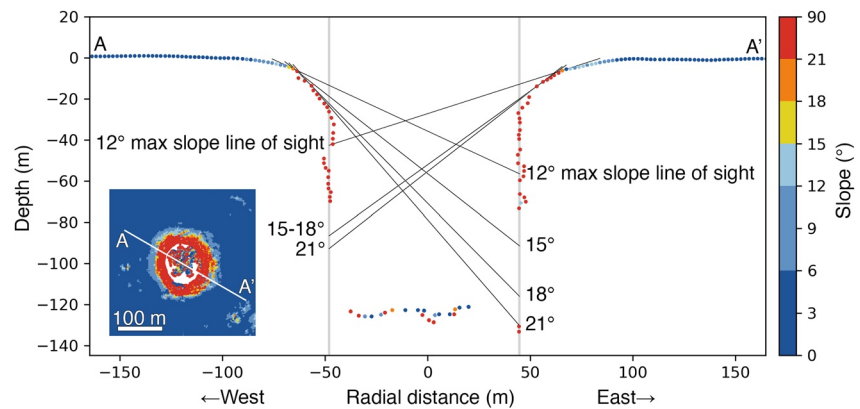


Figure 10. Profile across Mare Tranquillitatis pit, showing radial slope values and line of sight to wall for a vehicle with a 2 m vertical camera mast, and maximum slope traversal abilities between 12° and 21°. Inset map shows radial-direction slopes and profile location.

We constrained the ages of mare pits to between 50 and ~3.5 billion years. By comparison with the apparent degradation rate of impact melt pits, we infer that the vertical walls of even large pits become significantly eroded, exiting the youngest degradation categories (1 and 2) over a few hundred million years. By ~3 by of age (the maximum age of the highly degraded Mare Insularum pit), pits will likely be so degraded that it may be difficult to distinguish them from impact craters (category 5, or even more degraded). Based on their crisp appearances, highland pits may generally be younger, and possibly shorter-lived, though we cannot say by how much.

8. Exploration Considerations

Numerous scientific and engineering questions can be addressed by investigating the interiors of pits, from the size and origin of any cave, to the history of mare formation exposed in the walls. The less-degraded pits (e.g., MHP, MTP) likely present the best opportunity to investigate potential caves, and have large expanses of layered vertical walls. However, exploring them will be challenging, and more-degraded pits may offer easier pit entry using conventional exploration techniques. We will discuss the exploration challenges of funnels, overhanging walls, and rubble piles using the morphologic reconstruction presented here and using conventional and emerging techniques to overcome those challenges.

Funnels could be difficult for a non-specialized rover to traverse safely. We modeled the lines of sight along radial traverses toward the rims of MTP and MIP for safe traversable angle limits between 12° and 21°, assuming a 2 m vertical camera mast. We have found that rovers must be able to traverse slopes >15° to see more than ~2/3rds of the way down the pits in most places, and some sections of the lower walls may never be visible without traversing slopes >21° (especially MTP's west wall; Figure 10). Approaching close enough to see the floor or to access the uppermost coherent layers directly would likely require a tethered rover (e.g., Nesnas et al., 2019), as the lowest slopes of the funnel are frequently above the angle of repose of loose regolith and may not be stable under the weight of a rover.

A flying vehicle (e.g., Kalita et al., 2018; Martin et al., 2022; Robinson et al., 2014) could bypass the funnel slopes and avoid complications from forces on the tether dislodging funnel material that could fall onto the rover. However, such a vehicle would be limited to remote observations of the walls unless it can land on near-vertical surfaces.

Direct physical access to wall surfaces is challenging. A descender that is anchored by a tether from above (e.g., Nesnas et al., 2019) can traverse vertical walls, but it may be unable to contact overhung surfaces that are recessed from the most-protruding layer. Free-climbing vehicles supported by clinging to wall surfaces (e.g., Parness et al., 2017) would need to navigate both complex rock overhangs and coatings of dust or thicker regolith on upward-facing surfaces that may affect their rock-climbing mechanisms.

For the least-degraded pits (states 1–2, e.g., MHP and MTP), close-range remote sensing during descent may be the best approach for investigating wall materials, as navigating the rough and frequently overhung walls will be

challenging. The easiest access to wall materials occurs in more degraded pits (state 3), where there is at least one wall with minimal overhangs, such as the east wall of MIP or the upper south wall of LMP. However, these easier-to-access non-overhung walls may have a veneer of loose regolith that would hinder compositional measurements without a mechanism to expose the underlying bedrock.

Exploring a sublunarean void extending significantly under the mare will be challenging; the observer may need to climb or land on top of a several-meter-high pile of blocky debris toward the side of the floor to have visibility into the extended void space. Additionally, pits with a deep vertical shaft above any overhang imply that a large amount of material collapsed into the original void space during formation. As we have ruled out the presence of flowing magma during formation to carry away collapsed roof material, that collapsed material will still lie jumbled within the void, filling more space than the now-missing roof and possibly blocking access to any caves (Okubo et al., 2013).

9. Discussion and Conclusions

The reconstruction of pit morphology presented here shows that pits are defined by: (a) sloping transition from mare surface (near the angle of repose and varying in depth around the perimeter of a pit) ending abruptly at (b) a nearly vertical wall that (c) sometimes leads to an overhang (that hides the floor to wall contact). Furthermore, (d) the floors of all pits exhibit debris that likely was derived from the pit wall and surrounding mare surface. Additionally, we attribute significant morphologic variations from pit to pit to erosional processes over time.

Several lines of evidence point to ages for mare and highland pits of <1 by. Lack of correlation between host material age and pit degradation, along with the small scale of pits relative to the equilibrium diameter of craters in their host material, suggests that the pits formed well after mare formation. Small craters provide evidence of geologically recent erosion, with few craters seen within pits, and a crisp crater on the rim of MHP that appears to have been modified after formation by expansion of the pit rim. Finally, from morphologic and scale similarities of these pits to impact melt pits, which occur almost exclusively in Copernican craters (<1 Ga), we infer that mare and highland pits likely survive for <1 by. Although mare pits cannot have formed as skylights to active lava tubes, they could have formed as collapses into tubes, or into other ancient sublunarean voids, long after the eruption ceased.

Using the range of highland and mare pit morphologies documented here and the degradation scale we derived, we determined the most likely candidate for pit formation is an upwardly-eroding open void of indeterminate origin. Determining the nature of these voids remains elusive, and volcanic, isostatic, and tectonic forces have been invoked as origins (Robinson et al., 2012; Sauro et al., 2020; Wagner & Robinson, 2014; Wilson et al., 2011).

The two Marius Hills pits are co-located with volcanic landforms exhibiting high discharge events, consistent with lava tube formation. North Procellarum 1 and 2 are also located near high-discharge volcanic features, and their relative proximity and orientation suggest formation into the same subsurface void. These four pits are potential examples of collapses into lava tubes.

The highland pits are a bit mysterious, as there are only five, and they are small relative to the resolution of the LROC NAC, making it difficult to identify details. However, their general morphology and co-location with tectonic and volcanic features indicate they may have similar void formation mechanisms to the mare pits. The lava tube collapse hypothesis is unlikely to be viable for highland pits, but the relatively close distance from the mare could produce voids from intrusive magmatism or tectonic activity. Current orbital evidence is insufficient to unambiguously distinguish between collapse into lava tubes, other magmatic features, or tectonically formed voids.

Comparing the geologic setting and detailed morphology of lunar pits with that of terrestrial pits is an important step in setting out goals, objectives, and challenges before entering a pit. We believe that the most significant outstanding questions concerning mare pits, prioritized from simplest to most complex for a mission to address, are: (a) how large is the void; (b) how stable is the void; (c) how did the void form; and (d) other scientific issues whose study can be supported by pits (e.g., mare flow thicknesses, paleo-regolith formation, magma compositional evolution over time) (Figure 11).

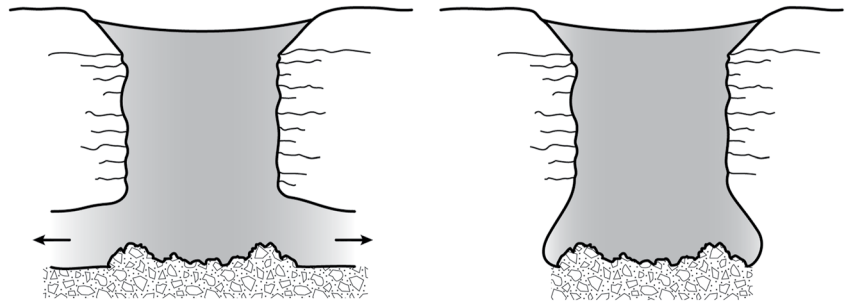


Figure 11. Collapse into an extant lava tube (left) or collapse into a small magmatic or tectonic void (right) are the two leading hypotheses for mare pit formation; each has very different exploration implications. A mission designed to test these two hypotheses could also acquire measurements to address other significant science questions.

The three best candidates for near-term exploration to answer these questions are LMP, MIP, and MTP. LMP has a smooth $\sim 21^\circ$ slope from rim to floor on one side, possibly allowing a vehicle access to the entire depth, and, if extant, any opening to a sublunarean void, although there is little evidence to support such an opening. MIP, on the lunar far side, has a stair-step series of short vertical exposures on the east wall, with minimal overhangs, and a large overhung region to the southwest. Traversing the floor would require navigating a dense field of boulders, however, and any remaining cave access is small. MTP is the least traversable of the three, with significant overhung recesses even in the vertical sections of its walls, but is much more likely to have an extant opening to the void it collapsed into and, uniquely among the mare pits, has direct line-of-sight to Earth from parts of the floor (Robinson et al., 2014). A fourth commonly proposed destination, MHP, is similar to MTP, but exposes a smaller extent of layered deposits than any of the three best candidates, and is less likely than MTP to have cave access.

Mare pit exploration is motivated by significant science and exploration questions. The pits present a variety of engineering challenges due to their complex morphology (steep walls, overhangs, rubble-covered floors, and potentially loose wall material). The detailed pit reconstructions presented in this study lead us to conclude that no single mission architecture can address all the open questions. We propose that the most compelling question is the extent of sublunarean voids. Thus, we propose that the first pit exploration mission focuses on that question with a low-cost flying vehicle that enters a relatively fresh pit and surveys its hidden regions (lava tube vs. magmatic chamber collapse). Such a survey could answer that question (Figure 11), as well as provide detailed morphologic information and preliminary scientific data on other questions to assist in designing a focused follow-on mission. We propose that MTP is the best candidate for this first mission.

Data Availability Statement

The LROC NAC images and DTMs used in this study are publicly available through the Planetary Data System LROC Node. Search interfaces for images (“LROC PDS Search”) and DTMs (“LROC RDR Search”) are at <https://wms.lroc.asu.edu/>; data directories are at <http://pds.lroc.asu.edu/data/LRO-L-LROC-2-EDR-V1.0/> (images) and http://pds.lroc.asu.edu/data/LRO-L-LROC-5-RDR-V1.0/LROLRC_2001/DATA/SDP/NAC_DTM/ (DTMs) (Robinson, 2010, 2011). Apollo Panoramic Camera scans are publicly available at <https://wms.lroc.asu.edu/apollo/browse> (sets AS15 and AS16). Version 6.0.0 of ISIS used for data processing is archived at <https://zenodo.org/record/5347823> (Laura et al., 2022). The software, source images, and pit point clouds generated for this project have been archived at <https://doi.org/10.5281/zenodo.6622042> (Wagner & Robinson, 2022). The point clouds, along with any future updates or additional sites, will also be archived at the LROC PDS node as RDRs (Robinson, 2011).

Acknowledgments

Funding for this work was provided by the Lunar Reconnaissance Orbiter project. We would like to thank Madeleine Manheim for her work in ensuring the pits were detailed accurately in the public LROC DTMs. We would also like to thank Aaron Boyd for scientific discussions and Zachary Davis for proof-reading assistance. Finally, we would like to thank two anonymous reviewers, and the editors, for helpful comments and suggestions.

References

- Anderson, J. A., Sides, S. C., Soltesz, D. L., Sucharski, T. L., & Becker, K. J. (2004). Modernization of the integrated software for imagers and spectrometers. In *35th lunar and planetary science conference* (p.2039). abstract #2039. Retrieved from <https://www.lpi.usra.edu/meetings/lpsc2004/pdf/2039.pdf>
- Ashley, J. W., Robinson, M. S., Hawke, B. R., van der Bogert, C. H., Hiesinger, H., Sato, H., et al. (2012). Geology of the king crater region: New insights into impact melt dynamics on the Moon. *Journal of Geophysical Research*, 117, E00H29. <https://doi.org/10.1029/2011je003990>

- Blair, D. M., Chappaz, L., Sood, R., Milbury, C., Bobet, A., Melosh, H. J., et al. (2017). The structural stability of lunar lava tubes. *Icarus*, 282, 47–55. <https://doi.org/10.1016/j.icarus.2016.10.008>
- Blender Online Community. (2018). *Blender - a 3D modelling and rendering package* (Version 2.79 released in September 2017) [Computer software]. Stichting Blender Foundation. Retrieved from <http://www.blender.org>
- Chappaz, L., Sood, R., Melosh, H. J., Howell, J. C., Blair, D. M., Milbury, C., & Zuber, M. T. (2017). Evidence of large empty lava tubes on the Moon using GRAIL gravity. *Geophysical Research Letters*, 44(1), 105–112. <https://doi.org/10.1002/2016GL071588>
- Cintala, M. J., & McBride, K. M. (1995). Block distributions on the lunar surface: A comparison between measurements obtained from surface and orbital photography. *NASA Technical Memorandum 104804*. Retrieved from <https://ntrs.nasa.gov/citations/19960011631>
- CloudCompare. (2019). [GPL software]. (version 2.10) Retrieved from <http://www.cloudcompare.org/>
- Coombs, C. R., & Hawke, B. R. (1992). A search for intact lava tubes on the Moon: Possible lunar base habitats. In *Paper presented at the second conference on lunar bases and space activities of the 21st century* (pp. 219–229). NASA CP-3166.
- Cushing, G. E. (2012). Candidate cave entrances on Mars. *Journal of Cave and Karst Studies*, 74(1), 33–47. <https://doi.org/10.4311/2010EX0167R>
- Cushing, G. E. (2015). Mars global cave candidate catalog PDS4 archive bundle. *PDS Cartography and Imaging Sciences Node (IMG)*, 2(5), 7. <https://doi.org/10.17189/1519222>
- Cushing, G. E., Okubo, C. H., & Titus, T. N. (2015). Atypical pit craters on Mars: New insights from THEMIS, CTX, and HiRISE observations. *Journal of Geophysical Research: Planets*, 120(6), 1023–1043. <https://doi.org/10.1002/2014JE004735>
- Cushing, G. E., Titus, T. N., Wynne, J. J., & Christensen, P. R. (2007). THEMIS observes possible cave skylights on Mars. *Geophysical Research Letters*, 34(17), L17201. <https://doi.org/10.1029/2007GL030709>
- De Angelis, G., Wilson, J. W., Cloudsley, M. S., Nealy, J. E., Humes, D. H., & Clem, J. M. (2002). Lunar lava tube radiation safety analysis. *Journal of Radiation Research*, 43, S41–S45. <https://doi.org/10.1269/jrr.43.S41>
- Edmundson, K. L., Cook, D. A., Thomas, O. H., Archinal, B. A., & Kirk, R. L. (2012). Jigsaw: The ISIS3 bundle adjustment for extraterrestrial photogrammetry. *ISPRS Annals of Photogrammetry, Remote Sensing and Spatial Information Sciences*, 14, 203–208. <https://doi.org/10.5194/isprsannals-14-203-2012>
- Fagents, S. A., Elise Rumpf, M., Crawford, I. A., & Joy, K. H. (2010). Preservation potential of implanted solar wind volatiles in lunar paleoregolith deposits buried by lava flows. *Icarus*, 207(2), 595–604. <https://doi.org/10.1016/j.icarus.2009.11.033>
- Favre, G. (1993). Some observations of Hawaiian pit craters and relations with lava tubes. In *Proceedings of the 3rd international symposium of vulcanospeleology* (pp. 37–41). Retrieved from <http://www.vulcanospeleology.org/sym03/ISV3x08.pdf>
- Greeley, R. (1971). Lava tubes and channels in the lunar Marius Hills. *The Moon*, 3(3), 289–314. <https://doi.org/10.1007/BF00561842>
- Halliday, W. R. (1966). Terrestrial pseudokarst and the Lunar topography. *National Speleological Society Bulletin*, 28(4), 167–170. Retrieved from <https://caves.org/pub/journal/NSS%20Bulletin/vol%2028%20part%204.pdf>
- Haruyama, J., Hara, S., Hioki, K., Morota, T., Yokota, Y., Shirao, M., et al. (2010). New discoveries of lunar holes in mare Tranquillitatis and mare Ingenii. In *41st lunar and planetary science conference*. abstract #1285. Retrieved from <https://www.lpi.usra.edu/meetings/lpsc2010/pdf/1285.pdf>
- Haruyama, J., Hioki, K., Shirao, M., Morota, T., Hiesinger, H., Miyamoto, H., et al. (2009). Possible lunar lava tube skylight observed by SELENE cameras. *Geophysical Research Letters*, 36(21), L21206. <https://doi.org/10.1029/2009GL040635>
- Heacock, R. L., Kuiper, G. P., Shoemaker, E. M., Urey, H. C., & Whitaker, E. A. (1966). *Ranger VIII and IX Part II. Experimenters' analyses and interpretations*. JPL Technical Report 32–800. Retrieved from <https://ntrs.nasa.gov/citations/19660015757>
- Henriksen, M. R., Manheim, M. R., Burns, K. N., Seymour, P., Speyerer, E. J., Deran, A., et al. (2017). Extracting accurate and precise topography from LROC narrow angle camera stereo observations. *Icarus*, 283, 122–137. <https://doi.org/10.1016/j.icarus.2016.05.012>
- Hiesinger, H., Head, J. W., Wolf, U., Jaumann, R., & Neukum, G. (2011). Ages and stratigraphy of lunar mare basalts: A synthesis. *Recent Advances and Current Research Issues in Lunar Stratigraphy*, 477, 1–51. [https://doi.org/10.1130/2011.2477\(01\)](https://doi.org/10.1130/2011.2477(01))
- Hiesinger, H., van der Bogert, C. H., Pasckert, J. H., Funcke, L., Giacomini, L., Ostrach, L. R., & Robinson, M. S. (2012). How old are young lunar craters? *Journal of Geophysical Research*, 117, E00H10. <https://doi.org/10.1029/2011je003935>
- Horvath, T., Hayne, P. O., & Paige, D. A. (2022). Thermal and Illumination Environments of Lunar Pits and Caves: Models and Observations from the Diviner Lunar Radiometer Experiment. *Geophysical Research Letters*, 49(14). <https://doi.org/10.1029/2022gl099710>
- Hörz, F. (1985). Lava tubes: Potential shelters for habitats. In *Lunar bases and space activities of the 21st century* (A86-30113 13-14) (pp. 405–412). Lunar and Planetary Science Institute. Retrieved from <https://adsabs.harvard.edu/pdf/1985lba.conf.405h>
- Kaku, T., Haruyama, J., Miyake, W., Kumamoto, A., Ishiyama, K., Nishibori, T., et al. (2017). Detection of intact lava tubes at Marius Hills on the Moon by SELENE (Kaguya) lunar radar sounder. *Geophysical Research Letters*, 44(20), 10155–10161. Portico. <https://doi.org/10.1002/2017GL074998>
- Kalita, H., Morad, S., Ravindran, A., & Thangavelautham, J. (2018). Path planning and navigation inside off-world lava tubes and caves. In *2018 IEEE/ION position, location and navigation symposium (PLANS)*. 1311–1318. <https://doi.org/10.1109/PLANS.2018.8373521>
- Laura, J., Acosta, A., Addair, T., Adoram-Kershner, L., Alexander, J., Alexandrov, O., et al. (2022). Integrated software for Imagers and Spectrometers [computer software]. Zenodo. <https://doi.org/10.5281/ZENODO.2563341>
- Martin, T. D., Atwell, M. J., Oelke, M. L., Crain, T. P., Robinson, M. R., Wagner, R. V., et al. (2022). S. P. Hopper: First in situ exploration of lunar polar terrain. In *53rd lunar and planetary science conference*. Abstract #2007. Retrieved from <https://www.hou.usra.edu/meetings/lpsc2022/pdf/2007.pdf>
- Masursky, H., Colton, G. W., & El-Baz, F. (1978). Apollo over the Moon: A view from orbit. *NASA SP-362*.
- Mazarico, E., Neumann, G. A., Barker, M. K., Goossens, S., Smith, D. E., & Zuber, M. T. (2018). Orbit determination of the lunar reconnaissance orbiter: Status after seven years. *Planetary and Space Science*, 162, 2–19. <https://doi.org/10.1016/j.pss.2017.10.004>
- Mylroie, J. (2019). Caves in space. *Journal of Cave and Karst Studies*, 81(1), 25–32. <https://doi.org/10.4311/2018ES0102>
- Nesnas, I. A., Kerber, L., Parness, A., Kornfeld, R., Sellar, G., McGarey, P., et al. (2019). Moon diver: A discovery mission concept for understanding the history of secondary crusts through the exploration of a lunar mare pit. In *2019 IEEE aerospace conference*. <https://doi.org/10.1109/aero.2019.8741788>
- Okubo, C. H., Cushing, G. E., & Titus, T. N. (2013). Mapping the cave and dike structure below Wood Valley pit crater, Kilauea Volcano, Hawai'i. In *2nd international planetary caves conference*. Abstract #9005. Retrieved from <https://www.hou.usra.edu/meetings/2ndcaves2015/pdf/9005.pdf>
- Okubo, C. H., & Martel, S. J. (1998). Pit crater formation on Kilauea volcano, Hawaii. *Journal of Volcanology and Geothermal Research*, 86(1–4), 1–18. [https://doi.org/10.1016/s0377-0273\(98\)00070-5](https://doi.org/10.1016/s0377-0273(98)00070-5)
- Parness, A., Abcouwer, N., Fuller, C., Wiltse, N., Nash, J., & Kennedy, B. (2017). LEMUR 3: A limbed climbing robot for extreme terrain mobility in space. In *2017 IEEE international conference on robotics and automation (ICRA)*. <https://doi.org/10.1109/icra.2017.7989643>
- Robinson, M. (2010). LRO MOON LROC 2 EDR V1.0 [Data set]. NASA Planetary Data System. <https://doi.org/10.17189/1520250>

- Robinson, M. (2011). LRO MOON LROC 5 RDR V1.0 [Data set]. NASA Planetary Data System. <https://doi.org/10.17189/1520341>
- Robinson, M. S., Ashley, J. W., Boyd, A. K., Wagner, R. V., Speyerer, E. J., Ray Hawke, B., et al. (2012). Confirmation of sublunarean voids and thin layering in mare deposits. *Planetary and Space Science*, 69(1), 18–27. <https://doi.org/10.1016/j.pss.2012.05.008>
- Robinson, M. S., Brylow, S. M., Tschimmel, M., Humm, D., Lawrence, S. J., Thomas, P. C., et al. (2010). Lunar reconnaissance orbiter camera (LROC) instrument overview. *Space Science Reviews*, 150(1–4), 81–124. <https://doi.org/10.1007/s11214-010-9634-2>
- Robinson, M. S., Lawrence, S. J., Close, W., Bode, R., Grunsfeld, J. M., Ingram, R., et al. (2008). The Apollo digital image archive. In *39th Annual lunar and planetary science conference*. abstract #1515. Retrieved from <https://www.lpi.usra.edu/meetings/lpsc2008/pdf/1515.pdf>
- Robinson, M. S., Thanga, J., Wagner, R. V., & Hernandez, V. A. (2014). Arne – Sublunarean explorer. *Annual Meeting of the Lunar Exploration Analysis Group* (Vol.1820, p. 3025). abstract #3025. Retrieved from <https://www.hou.usra.edu/meetings/leag2014/pdf/3025.pdf>
- Sauro, F., Pozzobon, R., Massironi, M., De Berardinis, P., Santagata, T., & De Waele, J. (2020). Lava tubes on Earth, Moon and Mars: A review on their size and morphology revealed by comparative planetology. *Earth-Science Reviews*, 209, 103288. <https://doi.org/10.1016/j.earscirev.2020.103288>
- Sides, S. C., Becker, T. L., Becker, K. J., Edmundson, K. L., Backer, J. W., Wilson, T. J., et al. (2017). The USGS integrated software for Imagers and Spectrometers (ISIS 3) instrument support, new capabilities, and releases. In *48th lunar and planetary science conference* (Vol.1964, p. 2739). Abstract #2739. Retrieved from <https://www.hou.usra.edu/meetings/lpsc2017/pdf/2739.pdf>
- Trask, N. J. (1966). Size and spatial distribution of craters estimated from Ranger photographs. In *Progress in the analysis of the fine structure and geology of the lunar surface from the Ranger VIII and IX photographs* (pp. 252–263). Jet Propulsion Laboratory Technical Report 32-800.
- Turner, R., & Kunkel, R. (2017). Radiation environment inside a lunar lava tube. In *47th international conference on environmental systems*. Retrieved from <http://hdl.handle.net/2346/72863>
- Wagner, R. V., Deran, A., & Robinson, M. S. (2017). Habitability and radiation environment within lunar pits. In *48th lunar and planetary science conference* (Vol.1964, p. 1202). abstract #1201. Retrieved from <https://www.hou.usra.edu/meetings/lpsc2017/pdf/1201.pdf>
- Wagner, R. V., & Robinson, M. S. (2014). Distribution, formation mechanisms, and significance of lunar pits. *Icarus*, 237, 52–60. <https://doi.org/10.1016/j.icarus.2014.04.002>
- Wagner, R. V., & Robinson, M. S. (2018). PitScan: Computer-assisted feature detection. In *Planetary science informatics and data analytics conference* (Vol.2082, p. 6051). Lunar and Planetary Institute. Abstract #6051. LPI Contribution No. 2082. Retrieved from <https://wufs.wustl.edu/psida/2018/abspres/pdf/6051.pdf>
- Wagner, R. V., & Robinson, M. S. (2019). 3D modelling of lunar pit walls from stereo images. In *50th lunar and planetary science conference*. abstract #2138. Retrieved from <https://www.hou.usra.edu/meetings/lpsc2019/pdf/2138.pdf>
- Wagner, R. V., & Robinson, M. S. (2021). Occurrence and origin of lunar pits: Observations from a new catalog. In *52nd lunar and planetary science conference* (Vol.2548, p. 2530). Abstract #2530. Retrieved from <https://www.hou.usra.edu/meetings/lpsc2021/pdf/2530.pdf>
- Wagner, R. V., & Robinson, M. S. (2022). Internal morphology point clouds of lunar pits [Data set and software]. Zenodo. <https://doi.org/10.5281/zenodo.6622042>
- Wagner, R. V., Robinson, M. S., Speyerer, E. J., & Mahanti, P. (2013). Topography of 20 km diameter craters on the Moon. In *49th lunar and planetary science conference*, (Vol.44, p. 2924). Abstract #2924. Retrieved from <https://www.lpi.usra.edu/meetings/lpsc2013/pdf/2924.pdf>
- Wagner, R. V., Rowland, S. K., & Robinson, M. S. (2018). Lunar pits and Hawaiian analogs. In *49th lunar and planetary science conference*. Abstract #1538. Retrieved from <https://www.hou.usra.edu/meetings/lpsc2018/pdf/1538.pdf>
- Wilcox, B. B., Robinson, M. S., Thomas, P. C., & Hawke, B. R. (2005). Constraints on the depth and variability of the lunar regolith. *Meteoritics & Planetary Sciences*, 40(5), 695–710. <https://doi.org/10.1111/j.1945-5100.2005.tb00974.x>
- Wilson, L., Hawke, B. R., Giguere, T. A., & Petrycki, E. R. (2011). An igneous origin for Rima Hyginus and Hyginus crater on the Moon. *Icarus*, 215(2), 584–595. <https://doi.org/10.1016/j.icarus.2011.07.003>
- Wolfram Alpha, L. L. C. (2017). WolframAlpha. access 19 Dec, 2017 <https://www.wolframalpha.com/>
- Wyryck, D. (2004). Distribution, morphology, and origins of Martian pit crater chains. *Journal of Geophysical Research*, 109(E6), E06005. <https://doi.org/10.1029/2004je002240>
- Yokota, Y., Haruyama, J., Yamamoto, S., Kaku, T., Matsunaga, T., Ohtake, M., & Michikawa, T. (2018). Formation scenario of continuous slopes associated with lunar mare pit/hole structures. In *49th lunar and planetary science conference* (Vol.2083, p. 1907). Abstract #1907. Retrieved from <https://www.hou.usra.edu/meetings/lpsc2018/pdf/1907.pdf>